Geophys. J. Int. (2006) doi: 10.1111/j.1365-246X.2006.02901.x

Core–mantle boundary structure investigated using *SKS* and *SKKS* polarization anomalies

Andrea Restivo* and George Helffrich

Earth Sciences, University of Bristol, Bristol BS8 1RJ, *UK. E-mail: arestivo@inogs.it*

Accepted 2005 December 17. Received 2005 December 2; in original form 2005 March 15

SUMMARY

Occasionally, *SKS* and *SKKS* waveforms in the same seismogram are affected differently by anisotropy. One source of this discrepancy may be structures in D″. In this study, we examine the discrepancy in order to determine where it arises in the propagation path and what it is due to. We find that D″ is the most likely source of the signal. The relatively minor differences in differential shear-wave splitting in *SKS* and *SKKS* limit large-scale azimuthal anisotropy in D″ to less than 2 per cent, though it may be locally stronger. The most effective way to develop the splitting differences is through polarization differences between *SKS* and *SKKS* imposed at the CMB. We examine how effective relief on and lateral gradients in CMB structure are at generating polarization anomalies and conclude that topography generates them best. Ramps and ridges are more effective generators of polarization anomalies than hills. Laterally extensive (500–1000 km) sloping CMB topography greater than 15° can develop the observed polarization anomalies in the data. The topography required exceeds constraints from other sources, so is unlikely to be the major factor explaining the anomalies. We produce a global map of *SKS*/*SKKS* exit points from the core where anomalous polarization behaviour is found, in relation to the velocity structure known to exist in D″: the anomalies appear to be restricted to faster than average areas of the CMB, suggesting a contribution from anisotropy related to the post-perovskite phase transition.

Key words: anisotropy, core–mantle boundary, hybrid method, lateral heterogeneity, polarization, shear-wave splitting.

1 INTRODUCTION

Bullen (1949) introduced the term D″ to identify the bottom few hundred kilometres of the mantle, which appeared to possess a different velocity gradient than the rest of the lower mantle (Gutenberg & Richter 1939). Since then, many seismological studies targeted the anomalous structure in this area (see the review by Loper & Lay 1995). Later investigations focused on characterizing the physical properties of D″ in order to infer the nature of the processes operating there. A consistent result emerging even from the earliest studies, is that D″ is laterally heterogeneous (Lay & Helmberger 1983). However, what is the horizontal scale length of this heterogeneity? This is the issue we address in the present work. An answer to this question may yield constraints on processes acting within D″ and on global phenomena affecting the mantle's lower boundary layer as diverse as chemical exchange between the iron-rich outer core and the silicate mantle (Meade *et al.* 1995; Knittle 1998), core–mantle coupling's role in the generation of the geomagnetic field and its observed secular variation (Poirier *et al.* 1998; Holme 1998), the convective style of the mantle (Williams *et al.* 1998; Sidorin & Gurnis 1998; Tackley 1998).

While the studies of D″ properties are legion, the methods used to date to explore its structure are relatively few, comprising reflections and mode conversions from inferred discontinuities (Lay & Helmberger 1983; Mori & Helmberger 1995; Olivieri *et al.* 1997), waveform modelling (Garnero & Helmberger 1995; Ni & Helmberger 2001), scattering (Hedlin *et al.* 1997; Earle & Shearer 1997; Vidale & Hedlin 1998; Thomas *et al.* 1999), anisotropy (Kendall & Silver 1996; Kendall & Nangini 1996; Thomas *et al.* 2002; Garnero & Lay 2003) and travel time anomalies (Lay *et al.* 1997; Kuo *et al.* 2000; Tkalcic *et al.* 2002).

For the purposes of characterizing lateral heterogeneity, *SKS* and *SKKS* are suitable probes of D″ because their steep paths through the mantle provide good lateral resolution at the bottom of the mantle. Both their traveltimes and their polarizations can be exploited. In this study we focus on polarization and splitting due to anisotropy. The *P–SV* conversion at the CMB exit point polarizes both phases, and thus polarization anomalies may be associated with near-CMB phenomena. Ray theory in a spherically symmetric earth model

*Now at: Ist. Naz. di Ocean. e di Geofis. Sper.—OGS, Centro di Ricerche Sismologiche, via Treviso 55, Udine, Italy.

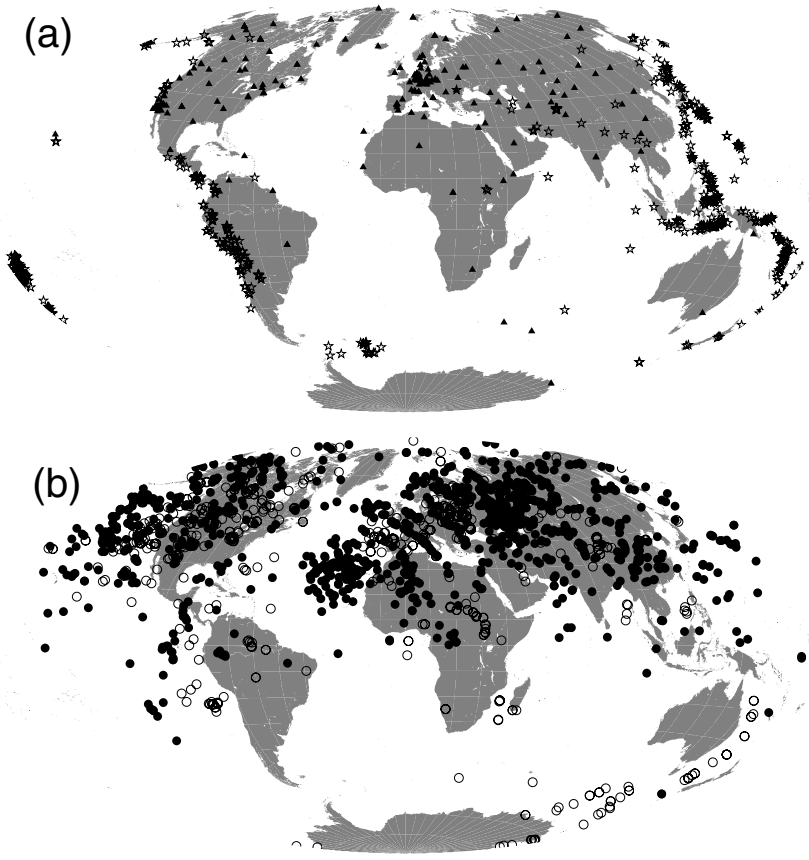

Figure 1. (a) Map of stations used and CMB sampling in the study. Triangles indicate GDSN, CNSN, ORFEUS, Geoscope and other FDSN stations used in the analysis. Stars indicate earthquake epicentres. (b) Map of CMB emergence points of *SKS* and *SKKS*, shown as open and full circles, respectively. These occur in pairs extending along the source–receiver arc because our method considers only seismograms containing both *SKS* and *SKKS* arrivals.

predicts that both *SKS* and *SKKS* will be polarized in the source–receiver plane, and thus they should have identical splitting due to upper mantle anisotropy, which, observationally, is largely independent of slowness and azimuth (Silver 1996). Any discrepancy found to this behaviour should flag anomalous structure encountered at the CMB which could exist as either azimuthal anisotropy or lateral velocity gradients (see also recent works by Perez & Niu 2004 and Hall *et al.* 2004). Either can deflect the original polarization planes inherited at the *P–SV* conversion at the CMB. The phases sample different areas of the CMB before converging to their common receiver with almost identical paths in the mid and upper mantle. Thus any relative polarization anomalies can reasonably be attributed to the differently sampled regions of D″ having different properties.

We find in a study of differential *SKS* and *SKKS* splitting that azimuthal anisotropy in D″ is not widespread, since the two phases' splitting parameters do not significantly differ. This implies that either D″ is largely isotropic or hexagonally anisotropic, with the symmetry axis vertical. This results is confirmed by a similar global investigation of waveform splitting of *SKS* and *SKKS* on the same record, which exploits a different analysis approach than ours (Perez & Niu 2004). Conversely, Hall *et al.* (2004) focus on physical models of D″ azimuthal anisotropy to plausibly explain *SKS* and *SKKS* discrepant splitting. We also find that significant polarization anomalies are uncommon, occurring in about 5 per cent of the observations. The locations at the CMB where the anomalies arise do not seem to be in regions of thick low-velocity structures at the CMB.

To explain these results, we propose a simple model—topography on discontinuities at or near the CMB—for the cause of polarization rotations. Through the polarization analysis of finite-frequency synthetic seismograms we show that this model is capable of explaining the observed polarization anomalies with topographic differences as small as 50 km over lateral distances as small as 500 km.

2 DATA AND METHODS

2.1 Data sources

The seismograms for the study are broad-band records of about 16 000 *SKS* and *SKKS* waveforms at distances $\geq 85^\circ$ and with $m_b > 5.0$ from the Global Digital Seismic Network, the Canadian National Seismic Network, ORFEUS, Geoscope and other FDSN sources between 1981 and 1997. Winnowing of the raw data set using the signal-to-noise (S/N) ratio, clarity of *SKS* and *SKKS* and strict separation in time of each arrival reduced the number to about 1800 seismograms. A map of the CMB coverage and stations used is shown in Fig. 1.

2.2 Analysis methodology

The key indication of anomalous behaviour is a difference in splitting between *SKS* and *SKKS* on the same seismogram. The variant of the Silver & Chan (1991) method we use to measure splitting minimizes the energy on the tangential component of the rotated

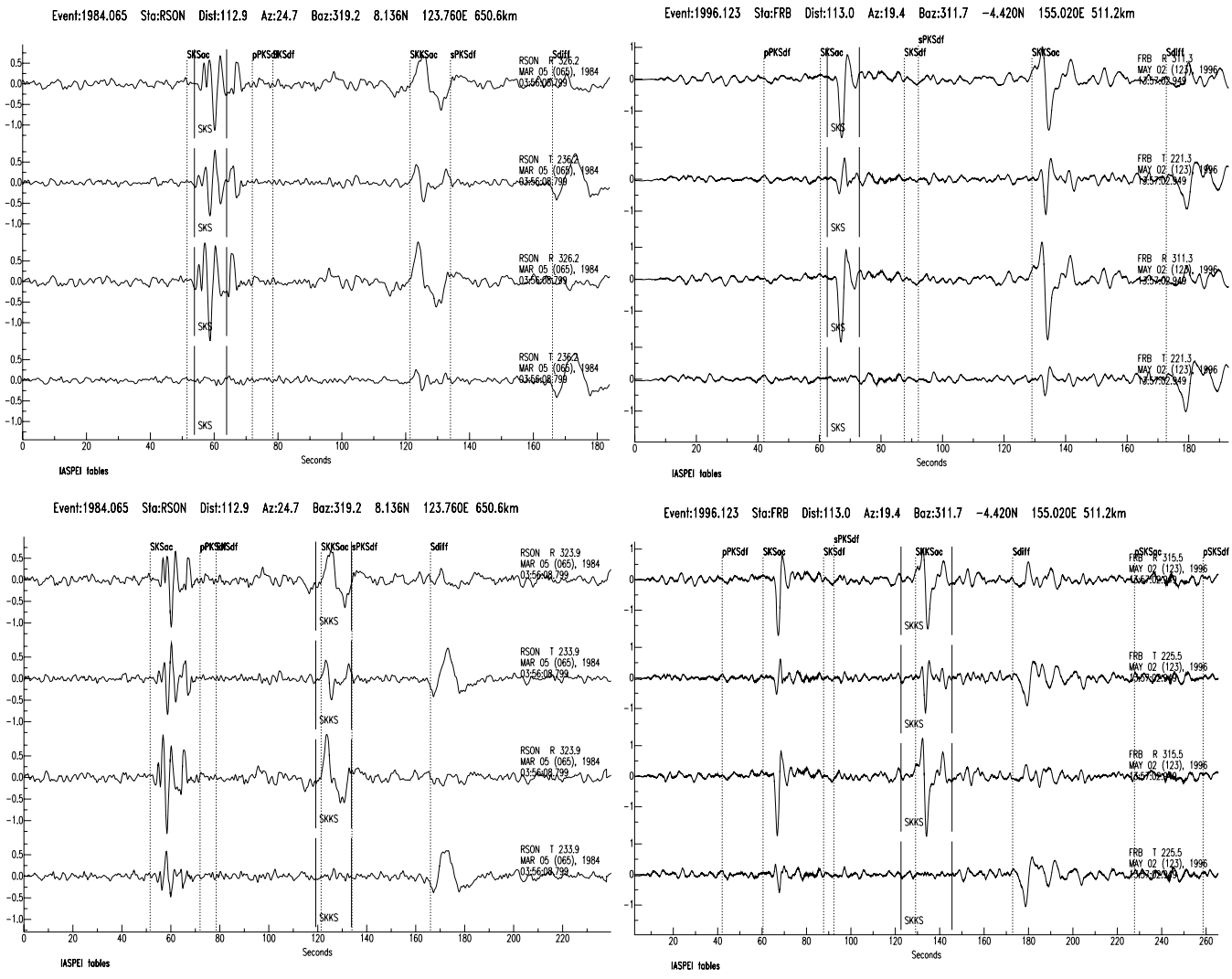

Figure 2. Anomalous splitting observed at RSON (*left*) and FRB (*right*). Radial and tangential components are shown before and after the application of an inverse splitting operator derived for *SKS* (*top*) and *SKKS* (*bottom*). In each panel, each pair of traces shows the radial and tangential component of the seismogram before the inverse splitting operator is applied (top pair) and afterwards (bottom pair). In both cases the splitting is not removed from the other phase. Dotted vertical lines represent the expected phase arrivals from IASPEI tables; solid vertical lines delimit the splitting analysis window.

seismograms by finding the eigenvalues of the horizontal particle motion. We assume splitting is due to a single anisotropic layer on the basis of the rarity of demonstrable multiple-layer splitting (Silver 1996). The measurement yields not only estimated splitting parameters ϕ and δt (ϕ is the fast polarization direction, and δt is the lag time between arrivals polarized in the fast and slow directions), but also an estimate of the polarization of the incoming shear wave before interacting with the anisotropic medium. Each measurement also yields an inverse splitting operator that restores the observed waveforms to their state before entering the anisotropic region. If splitting of *SKS* differs from *SKKS*, the inverse splitting operator for one of the arrivals does not properly act on the other. Two examples of such anomalous measurements are illustrated in Fig. 2 for two different paths to North American stations.

2.3 Resolution

One parameter we will be estimating in the subsequent analyses of *SKS* and *SKKS* records is the incoming polarization of the shear wave ϕ_i before it interacts with the anisotropic medium. The uncertainty in the estimate depends on the S/N level in the trace. In earlier work, we undertook numerical experiments with synthetic seismograms to explore the dependence of ϕ and δt retrieval on noise levels (Restivo & Helffrich 1999).

As before, we define the S/N ratio for an *SKS* or *SKKS* splitting measurement by the ratio of the maximum amplitude of the signal on the radial component inside the measurement window and the 2σ value of the amplitude on the tangential component in the same measurement window after the appropriate inverse splitting operator has been applied to it. We next generated a number of synthetic seismograms with the dominant signal frequency of *SKS* (0.125 Hz) at six different noise levels for different fast polarization direction orientations ϕ and delay times δt. In each synthetic, the backazimuth ϕ_b was 0°. We processed these records using the same analysis methodology as for our real data and estimated the initial polarization direction ϕ_i. To account for the different visibility of such splitting on tangential components of records and the possible influence this factor may have on initial polarization measurements, the suite of synthetic waveforms included different angles between ϕ and backazimuth: 10°, 20°, 30° (the behaviour has $\pi/4$

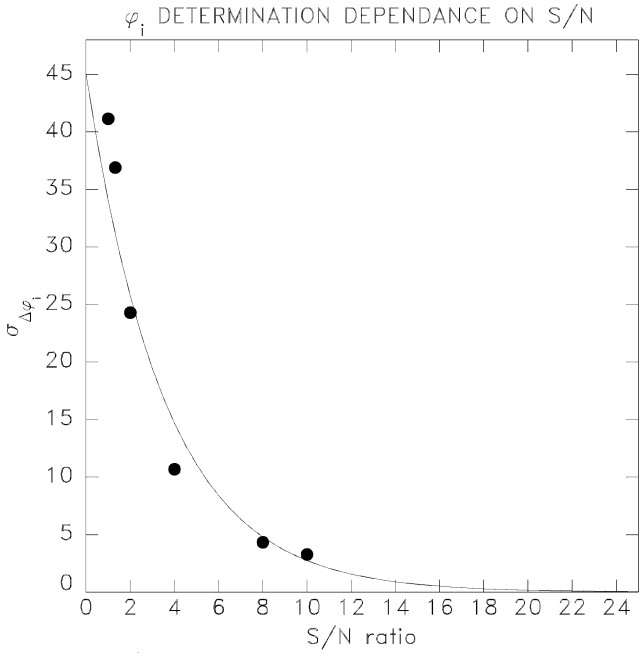

Figure 3. Summary of synthetics for retrieval of ϕ_i with different noise levels, backazimuth deviations from the fast polarization direction ϕ_b, and splitting parameters (ϕ, δt). The average synthetic $\sigma_{\Delta\phi}$ values vs S/N ratio follow an exponential distribution simply parametrized as $\sigma(x) = a\ \exp(-bx)$, where x is the S/N ratio. A fit to the average values with the constraint $a = 45^\circ$ yields $b = 0.279885$.

symmetry). Our results show that for a given δt, initial polarizations may be retrieved more accurately with increasing separation of ϕ_b from ϕ. A smaller spread in σ_{ϕ_i} is seen for increasing δt at any given S/N ratio. The cumulative σ_{ϕ_i} results at all S/N levels tested are shown in Fig. 3 together with the function which best interpolates them. This curve provides us with a way to estimate the measurement uncertainty for ϕ_i from the S/N ratio of the splitting measurement. The trend may be summarized using the following rule of thumb: for S/N > 7:1, incoming polarization rotations of *SKS* and *SKKS* from the backazimuth direction can be determined within a 6° uncertainty irrespective of splitting parameters.

3 RESULTS

3.1 Causes of anomalous splitting

Splitting of *SKS* and *SKKS* should be virtually identical because both are polarized in the source–receiver plane by the *P*-to-*S* conversion at the CMB and because their paths through the upper mantle are similar. Observationally, anisotropy is concentrated at levels above the transition zone in the upper mantle (Meade *et al.* 1995; Fouch & Fisher 1996) which should affect *SKS* and *SKKS* similarly. Regional anisotropy is known immediately below 660 km (Wookey *et al.* 2002) but appears to have hexagonal (azimuthal) symmetry, which will not affect vertically travelling waves such as *SKS* and *SKKS*. Horizontally travelling shear waves through D″ also locally show anisotropy (Kendall & Nangini 1996; Thomas *et al.* 2002; Garnero & Lay 2003), but, for vertical paths through D″, its effect must be minor in comparison to the upper mantle's because anisotropy in *SKS* and *SKKS* is strongly related to lithospheric tectonic history (Silver & Chan 1991; Silver 1996; Barruol *et al.* 1997). Thus anomalies in *SKS* and *SKKS* splitting behaviour are likely to arise at the CMB or near it in D″, where their paths are most widely separated.

There are two plausible explanations for differences in *SKS* and *SKKS* splitting. The first is azimuthal anisotropy in D″, which is suggested by differences in *SH* and *SV* wave speeds for diffracted *S* waves at the CMB (but vertical transverse isotropy also explains this). On account of different *SKS* and *SKKS* ray parameters, their emergence angles at the CMB may differ significantly enough to affect the *SV* polarization of *SKKS* due to SV's projection onto the vertical and horizontal symmetry axes of the anisotropic medium. Though subsequently split by upper mantle anisotropy, the aggregate splitting will differ on account of the anisotropy in D″. In particular we expect *SKS* and *SKKS* to show different delay times because of their different path lengths through D″; at 103° epicentral distance (average value in our data set) and assuming a 200-km-thick layer, *SKS* and *SKKS* have path lengths of 238 and 357 km, respectively.

The second explanation relies on differences in *SKS* and *SKKS* polarization inherited at the CMB. Though ideally *SV* polarized, the polarization may be rotated away from the *SV* plane by interacting with velocity gradients in D″ or topography at the CMB. A dipping interface at which a *P*-to-*S* conversion takes place (like the CMB might be), will rotate the polarization plane away from *SV* into the downdip direction on the conversion interface. If the two phases are differently polarized before undergoing splitting in the upper mantle, they will be split differently but yield the same splitting parameters for the anisotropic lithospheric layer they traverse. The concept is depicted in Fig. 4.

The key observation to discriminate between the two possibilities for anomalous splitting is whether the splitting parameters for *SKS* and *SKKS* are identical. We, therefore, assess their degree of similarity.

3.2 Observed delay times and fast-polarization directions

Fig. 5 shows the observed splitting parameters for *SKS* and *SKKS* where they appear in the same seismogram. The majority of records show very small differences, and in almost all cases they overlap at the 95 per cent confidence level. Similar conclusions follow from an examination of the delay times δt for *SKS* and *SKKS* measured from the same seismogram. There seem to be few occurrences of discrepant delay times. The data indicate that large-scale non-VTI anisotropy in D″ is absent.

Rarely, different splitting behaviour of *SKS* and *SKKS* arises, as shown in Fig. 2. In the FRB record *SKS* and *SKKS* δt differ at $>2\sigma$ level, even though the S/N ratios are high for each measurement (12:1 for *SKS* and 15:1 for *SKKS*). However, there is no significant difference in ϕ. δt for *SKKS* is larger than that for *SKS*, consistent with its longer path through D″ if azimuthal anisotropy is present at its exit point from the core. This region on the Arctic coast of Canada is indicated in Fig. 6, and lies within the broad area studied by Garnero & Lay (1997). Other *SKS* phases sampling nearby patches of the CMB are nonetheless unaffected. In combination with the general agreement of δt for *SKS* and *SKKS*, this observation suggests that non-VTI anisotropy in D″ is regionally localized.

Garnero & Lay (1997) infer and map VTI anisotropy in D″ beneath the North American continent as the general, long wavelength (>1000 km) structural pattern of the area from observations of $SH > SV$ velocities. As beneath the Caribbean (Kendall & Nangini 1996), this feature is associated with a sharp shear velocity discontinuity at the top of D″ and higher than average wave speeds in it. The long-period data and poor azimuthal sampling of the CMB,

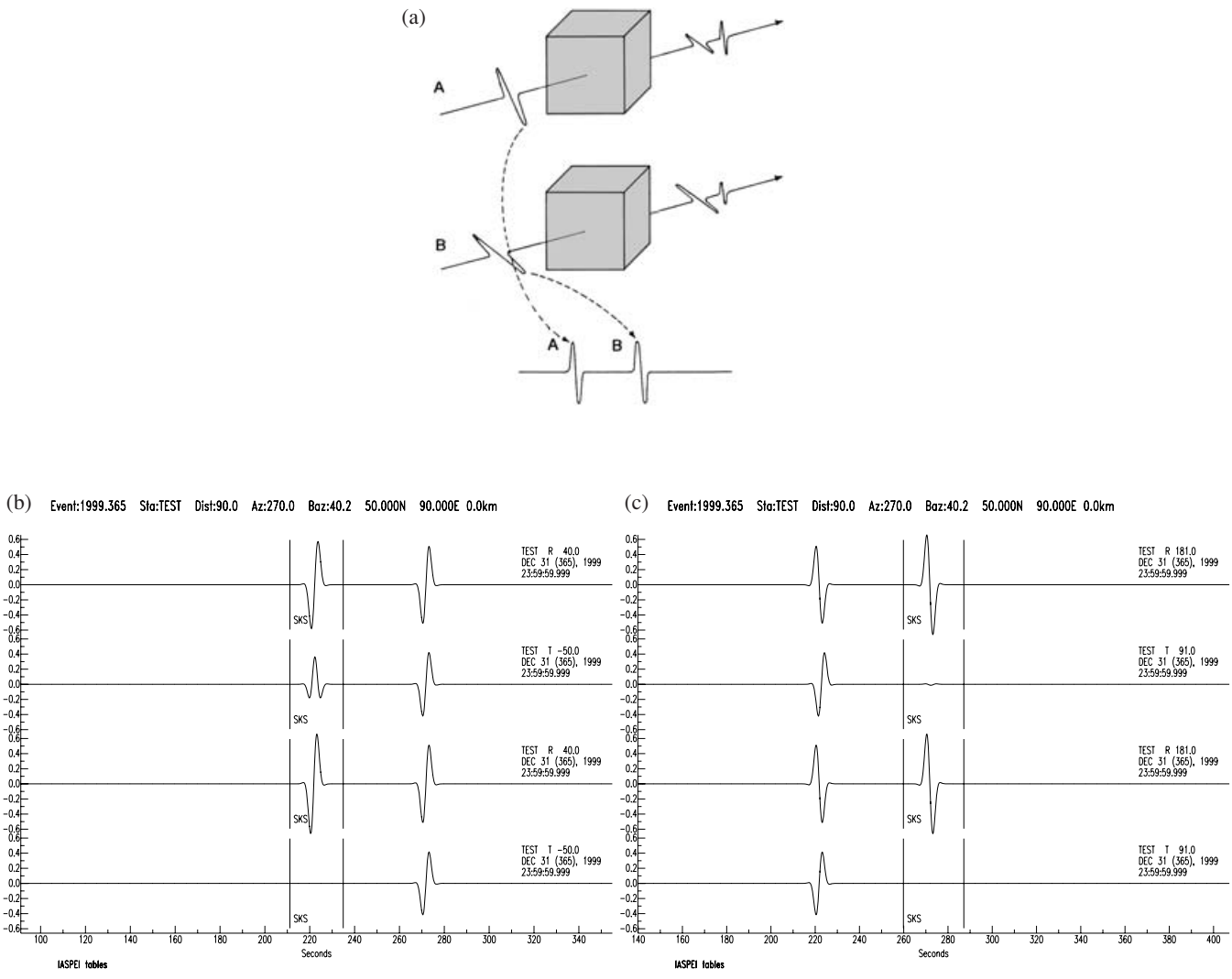

Figure 4. Motivation for differential *SKS* and *SKKS* splitting behaviour due to different initial polarization. (a) Wavelets A and B travel with very similar ray paths through the same anisotropic medium. The difference in the split waveforms is only due to their different original plane of polarization. (b, c) Splitting measurements for synthetic *SKS* and *SKKS* waveforms with different incoming polarization. *SKKS* is initially polarized along the backazimuth direction while *SKS* is rotated 40° away from it. Each pair of traces in each panel shows the radial and tangential component of the seismogram before the inverse splitting operator is applied (top pair) and afterwards (bottom pair). The inverse splitting operator calculated on *SKS* (b) and *SKKS* (c) does not remove the tangential energy of the other phase, yet identical splitting parameters (ϕ, δt) prevail for each arrival.

however, prevent them from finding any *SKS*/*SKKS* splitting that would imply azimuthal anisotropy at shorter and local scale, that we reveal. The authors further argue for lateral variations of the strength of transverse isotropy and of D″ thickness (thus D″ topography), diminishing and fading out westwardly. Indeed, *SKS* in our FRB record samples the area where such VTI anisotropy is stronger, undergoing no splitting in D″ while *SKKS* exits the core farther west, sampling an area of D″ that is mapped instead as slower than average by Williams *et al.* (1998).

We can estimate the maximum anisotropy from $\sigma_{\Delta\delta t}$ in our data. Viewing it as a bound on the differential splitting between *SKS* and *SKKS* accrued through a 200-km-thick anisotropic layer, the calculated δt difference should be smaller than $\sigma_{\Delta\delta t}$, which is 0.25 s (Fig. 5). The differential splitting $\Delta\delta t$ is, approximately,

$$\Delta\delta t = \frac{\Delta z}{v}\frac{\delta v}{v}\left(\frac{1}{\cos\theta_{\mathrm{SKKS}}} - \frac{1}{\cos\theta_{\mathrm{SKS}}}\right). \quad (1)$$

For a wave speed difference between the fast and slow axes $\frac{\delta v}{v}$ through a $\Delta z = 200$-km-thick D″ at an average source–receiver distance of 103°, the surface-source *SKS* and *SKKS* slownesses are 4.67 and 7.12 s/°, yielding angles θ_{SKS} of 32.8° and θ_{SKKS} of 55.7°. $\Delta\delta t$ is therefore 0.16 s for every percent of anisotropy in the 200-km-thickness interval. This limits the aggregate azimuthal anisotropy to less than 2 per cent throughout D″.

3.3 Initial polarization directions

We also examined our data for differences in initial polarization of *SKS* and *SKKS*, which, ideally, should be in the source–receiver plane. Station misalignment from north and east directions is a possible source of bias in these measurements. To correct for this, we removed the mean of the difference between the backazimuth and incoming polarization for all measurements made at each station. (This exercise (re-)discovered some previously reported significant misalignments such as RSNY (Owens 1987)). Fig. 7 shows the

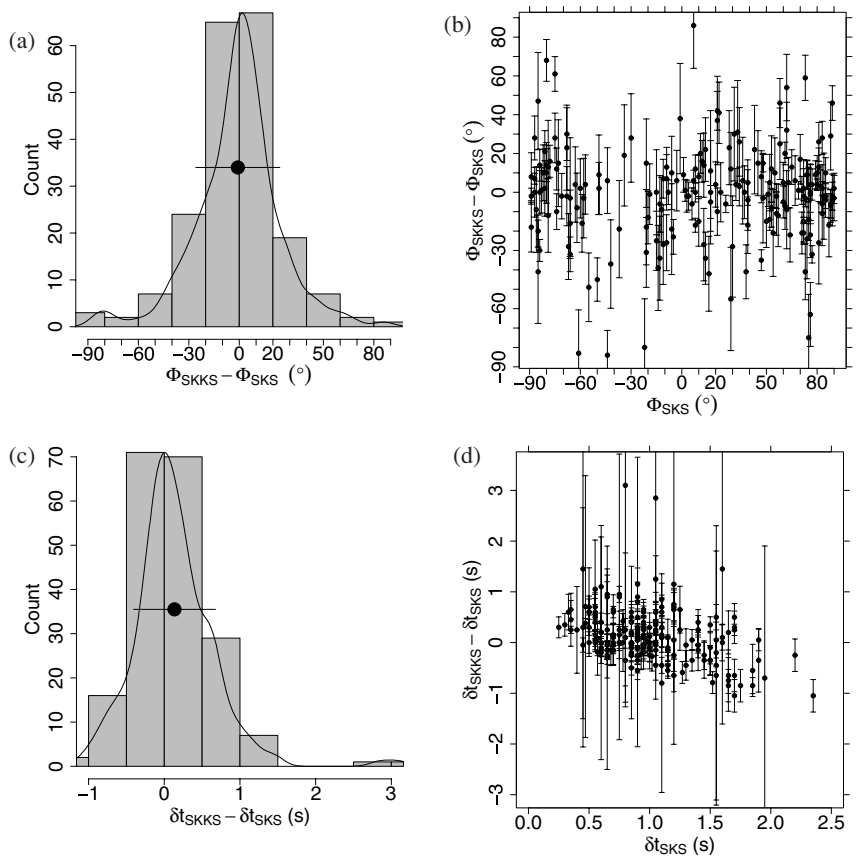

Figure 5. Splitting parameter differences for *SKS* and *SKKS* phases measured on the same seismogram. Histogram (a) shows difference between 197 $\phi_{\mathrm{SKKS}} - \phi_{\mathrm{SKS}}$ estimates from seismograms containing both *SKS* and *SKKS* arrivals. Graph (*b*) shows ϕ_{SKS} vs $\phi_{\mathrm{SKKS}} - \phi_{\mathrm{SKS}}$ deviations from the expected 1:1 relationship. Histogram (c) shows difference between 197 $\delta t_{\mathrm{SKKS}} - \delta t_{\mathrm{SKS}}$ estimates from seismograms containing both *SKS* and *SKKS* arrivals. Graph (*d*) shows δt_{SKS} vs $\delta t_{\mathrm{SKKS}} - \delta t_{\mathrm{SKS}}$ deviations from the expected 1:1 relationship. Bars indicate total uncertainty derived from 1σ errors of each measurement.

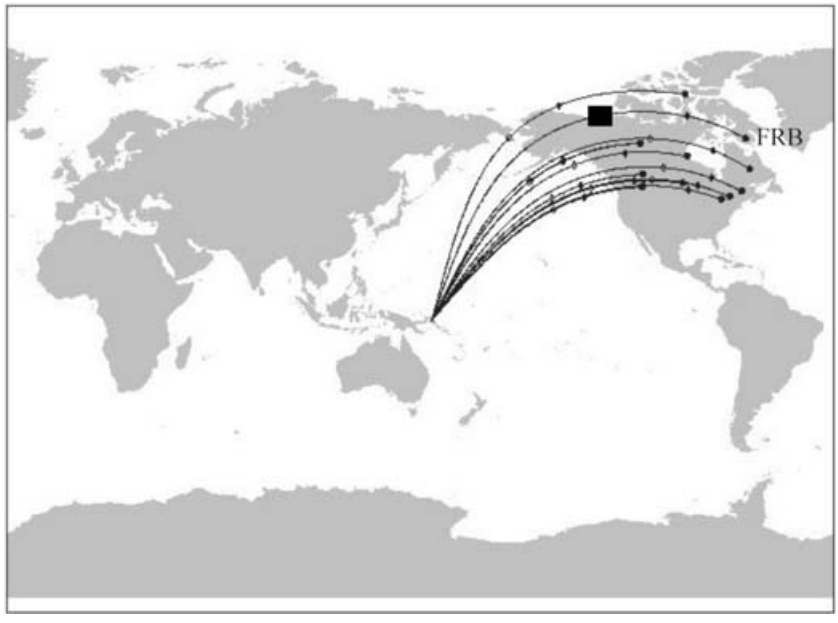

Figure 6. Ray paths for event showing anomalous splitting to Canadian and US stations. Black box identifies an area of inferred azimuthal anisotropy in D″ sampled by *SKKS* on leaving the CMB en route to FRB.

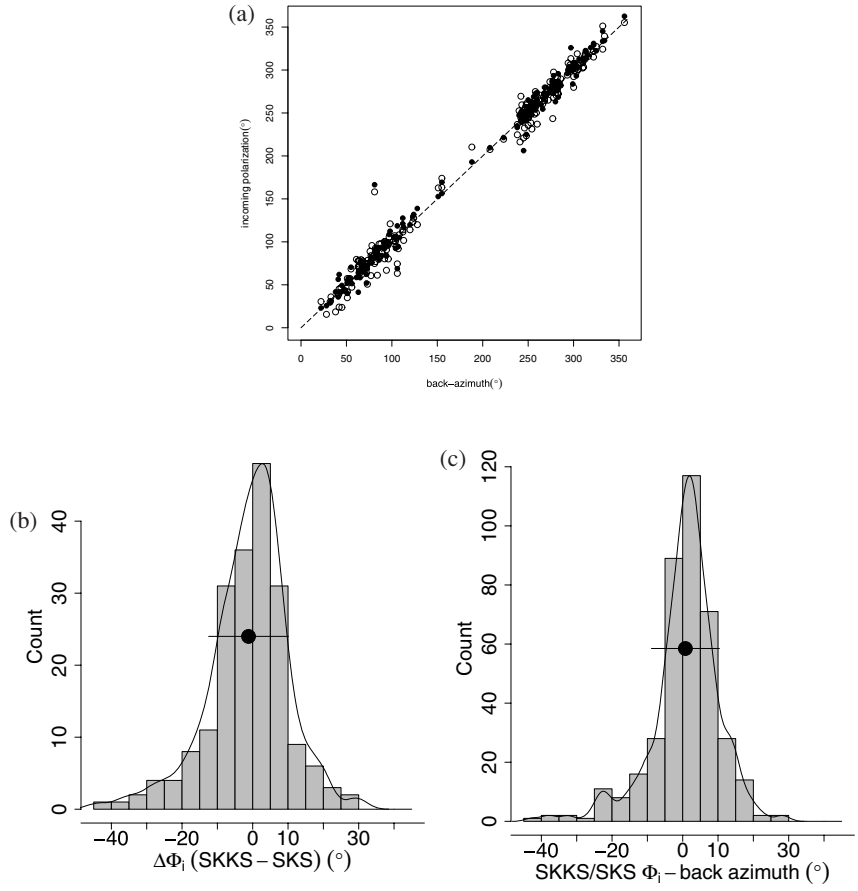

Figure 7. Estimated initial polarization directions for *SKS* and *SKKS* versus backazimuth. (a) • and ○ represent *SKS* and *SKKS* determinations respectively. For isotropic velocity structure, ray theory predicts phase polarizations in the source–receiver plane (dotted line) due to the *P-SV* conversion at the CMB. (b) Histogram of *SKKS-SKS* polarization differences. (c) Histogram of *SKKS* and *SKS* initial polarization estimates from backazimuth.

results. In contrast to splitting parameters themselves, polarization deviations show more anomalies on account of the robustness of the estimation method revealed by the synthetics. *SKKS* phases deviate more often and show larger displacements from the source–receiver plane than *SKS*.

While the misalignment correction forces $\Delta\phi_i$ to have zero mean, the standard deviations are 8.18° for *SKS* and 10.88° for *SKKS*. Polarization deviations in excess of these amounts are deemed 'anomalous'. The S/N ratios for the anomalous rotations are generally greater than 5:1 and range as high as 10:1 (*SKKS*) and 17:1 (*SKS*), indicating well-resolved differences by the criterion determined earlier with synthetics. The relative measurement reliability may be quantified by a confidence value C defined as

$$C = \left| \frac{\phi_i - \phi_b}{\sigma(\mathrm{S/N})} \right|, \tag{2}$$

where $\sigma(\mathrm{S/N}) = 45^\circ \exp(-0.279885 \times \mathrm{S/N})$, as found from the synthetics experiments. We projected the anomalous polarization rotations to the CMB emergence points of the associated phases, and show the distribution of C in Fig. 8. They delineate a broad area of the CMB laying under North America, with an extension into the northeastern Pacific, and an even more extensive region under Asia.

Using C provides an alternative way to classify anomalous incoming polarizations. Rather than defining an anomaly on the basis of the observed dispersion of $\phi_i - \phi_b$ as we did before, values of $C > 1$ may be used. These signify polarization rotations larger than the uncertainty at the observed S/N. This choice is a practical one: it provides a larger set of anomalous observations we may work with to examine their geographic distribution. There are 83 *SKS* and 70 *SKKS* observations with $C > 1$, distributed as shown in Fig. 9. There appears to be a spatial correlation between the geographical distribution of ULVZs as classified by Williams *et al.* (1998), and the CMB location of the *SKS* and *SKKS* polarization rotations that we observed: all but 8 North American rotated phases (which include the FRB anomalous *SKKS*) out of 153 confidently retrieved anomalously polarized *SKS*/*SKKS* emanate from CMB regions where ULVZs are absent. Four more come from ULVZ margins in Europe. This is an observation whose significance we will return to later.

4 ANALYSIS

4.1 Summary of observations

Widespread azimuthal anisotropy in D″ is not the main physical cause of the rare differential splitting we observed in seismograms for *SKS* and *SKKS*. Their splitting parameters coincide in most cases within standard measurement errors. Where it does exist, non-VTI anisotropy is only a small-scale, local feature. Large-scale azimuthal anisotropy in D″ seems to be limited to no more than the 2 per cent level (see also Hall *et al.* 2004). Differing incoming polarization of the two phases is more frequent than differing splitting

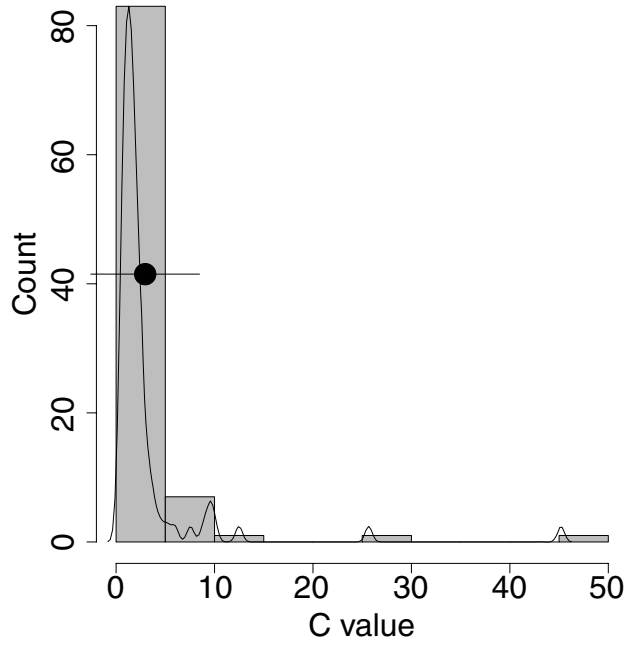

Figure 8. *C* distribution among 93 strongly anomalous polarization rotations, and their locations projected onto the CMB. (*Top*) Histogram of *C* values for anomalous polarization. (*Bottom*) Locations of strongly rotated ϕ_i projected onto their CMB exit points. Symbols indicate measurement reliability based upon *C*: ◯ - $C > 2.5$ (21 obs.); ○ - $1.5 \leq C \leq 2.5$ (33 obs.); ● - $C < 1.5$ (39 obs.) Lines indicate backazimuth directions at CMB. There are 40 *SKS* and 53 *SKKS* anomalies.

parameters. Similar conclusions for splitting are drawn in their study by Perez & Niu (2004). Differences with our work only regard the analysis method used. The authors in fact test for the match of observations with splitting arising from a two-parameter model (single anisotropic layer with its own ϕ and δt) and from a four-parameter one (two independent azimuthally anisotropic models). An F-test shows no mismatch improvement in using the double splitting model, except for records from just a handful of stations. The large majority of the lowermost mantle is thus, at most, transversely isotropic with laterally dipping structures.

4.2 Simple models of the CMB yielding polarization anomalies

4.2.1 Ray theory

What kind of structures or lateral velocity gradients in D″ are required to explain polarization anomalies like we observe for *SKS* and *SKKS*? And what length scales of velocity heterogeneity above the CMB may yield the range of polarization rotation values that we detect?

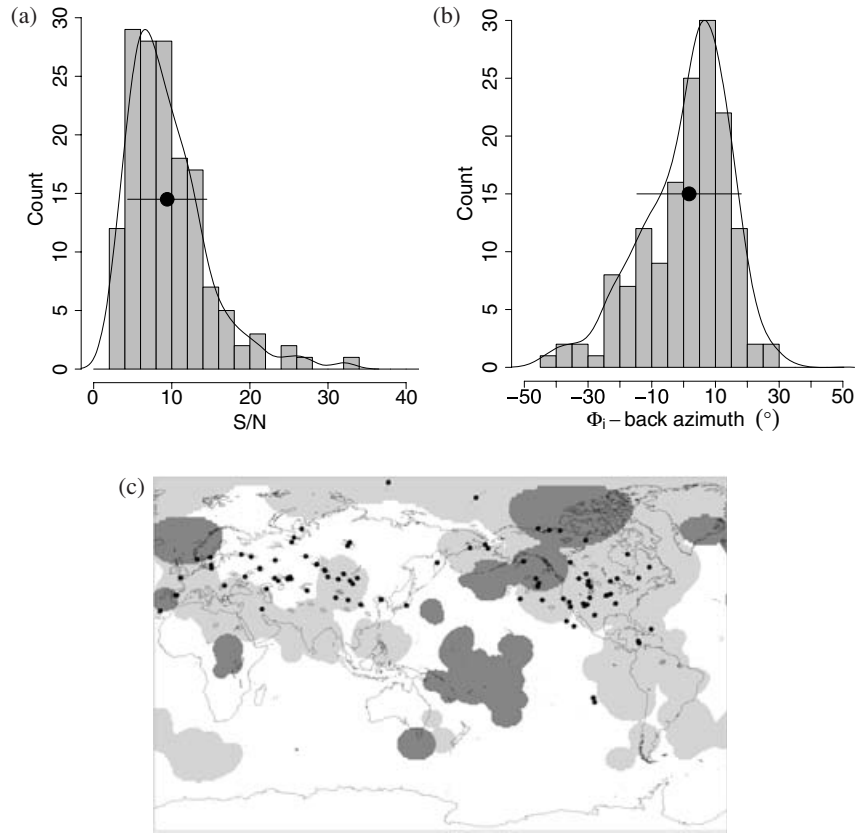

Figure 9. S/N ratio and polarization anomalies for observations with $C > 1$. (a) Histogram of S/N ratio values for the 153 observations. (b) Histogram of $\phi_i - \phi_b$ values for the same observations. (c) Anomalous *SKS* and *SKKS* polarizations projected onto the CMB exit points. Symbols indicate *SKS* (•) and *SKKS* (○) observations. Lines indicate backazimuth. Shaded regions are regions where ultra-low-velocity zones are observed (dark shading) and absent (light shading), or not known (no shading) (Williams *et al.* 1998).

To answer these questions we analyzed Kirchhoff synthetic seismograms containing *P*-to-*S* conversions at dipping 2- and 3-D interfaces (van der Lee *et al.* 1994). Kirchhoff synthetics are ideal for studying the interaction and propagation of a finite frequency wavefield because the far-field response is calculated as an integral over contributions from a surface, which we take to be the topographically deformed CMB.

When a polarized wave interacts with a seismic dipping discontinuity, ray theory prescribes that its plane of polarization will be deviated. For an *SKS* wave, the magnitude of the rotation is governed by the angular separation between the ray direction and the downdip direction on the interface. Thus, by examining the sense of rotation of an anomalous polarization rotation, the downdip direction may be inferred.

Examining the sketch plot in Fig. 10, we identify the mutually perpendicular unit vectors $\hat{s}$, $\hat{d}$ and $\hat{n}$ as the strike, dip and surface normal directions respectively that define the interface at the incidence point of a *P–SV* converted wave at the surface (which we assume to be the CMB). The unit vectors $\hat{e_u}$, $\hat{e_r}$ and $\hat{e_t}$ define the ray coordinate system consisting of the propagation direction of the transmitted shear wave and the radial and tangential components of its polarization. In a spherically symmetric earth *SKS* and *SKKS* are polarized in the source–receiver plane which contains $\hat{e_r}$ and $\hat{e_u}$. Polarization rotations out of this plane occur when the strike of the topography differs from the tangential direction of the shear wave arrivals. According to ray theory, the magnitude of this rotation Δ_i is $\cos^{-1}(\hat{d} \cdot \hat{e_r})$, the angle between $\hat{d}$ and $\hat{e_r}$ (Cerveny 2001).

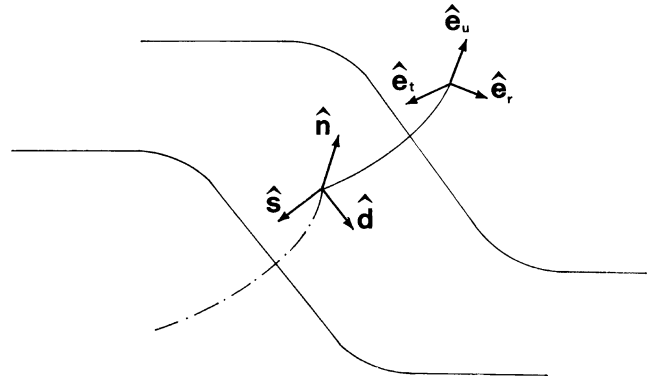

Figure 10. Sketch showing relevant geometry for ray-theoretic polarization anomalies induced by a dipping seismic discontinuity. $\hat{n}$, $\hat{d}$ and $\hat{s}$ indicate the discontinuity surface normal, downdip and strike directions, respectively. $\hat{e_i}$ indicate components of a ray-centred coordinate frame: radial ($\hat{e_r}$), tangential ($\hat{e_t}$), and longitudinal (or along-ray $\hat{e_u}$). The angle between $\hat{d}$ and $\hat{e_r}$ controls the polarization rotation of a *P*-to-*S* conversion at the interface.

4.2.2 Finite frequency

We used noise-free synthetics generated from 2- and 8-s period (τ) source wavelets to explore the interaction of a finite frequency wavefield with seismic velocity jumps at boundaries having different shapes, sizes and steepnesses. The synthetic *SKS* waveforms

Table 1. Input parameters to synthetic waves generating code for topographic CMB discontinuity (IASP91 of Kennett & Engdahl (1991)).

	Lower half-space (OC)	Upper half-space (LM)	Surface Source/Receiver
V_p (km s^{-1})	8.009	13.691	5.800
V_s (km s^{-1})	1×10^{-5}	7.302	3.360
ρ (g cm^{-3})	9.914	5.551	2.720

were produced using a code originally developed for $P_{660}s$ (van der Lee *et al.* 1994) with modifications. It employs an algorithm based on Kirchhoff–Helmholtz time-dependent surface integral representation of a scalar wavefield (Haddon & Buchen 1981). We used the properties of the outer core under the discontinuity and of the lowermost mantle above it. The half-spaces above and below the discontinuity are homogeneous, so *SKS* polarization rotations occur by the *P–SV* conversion rather than any lateral velocity gradients above the discontinuity. Table 1 lists the values used.

We can specify arbitrary 3-D topography on the interface and an arbitrary source–receiver geometry with respect to the interface as well. The average source–receiver distance in our data is 103°, which we used for all synthetics. At this distance, the ray theoretic *P*-to-*S* conversion point is 88° from the source for *SKS*. Travel times and ray parameters to all points on the conversion interface from the source were obtained by ray tracing through a spherical earth model (IASP91 of Kennett & Engdahl 1991) for a surface source. A 0.2° × 0.2° grid was used for the summation. Integration progresses in a circular neighbourhood around the minimum time point to reduce artefacts introduced by grid edges. A geometric spreading factor is also calculated from the simple Cartesian distance between the interaction point and the surface receiver and used to produce the final synthetic seismograms.

Test results are given in Figs 11(a) and (b) for 2 and 8 s period *SKS* synthetic waveforms for a dipping plane of infinite extent. Dipping seismic velocity boundaries do produce rotations of the polarization direction also for wavefields with finite frequency. In general, induced deflections depend on the interface's slope. They also depend on the backazimuth separation from the downdip direction and approach ray-like behaviour in the limiting case of small differences between $\hat{d}$ and $\hat{e}_r$ and for increasing slope. As it can be expected from lateral averaging at longer periods, 8 s synthetics incur less polarization rotation than 2 s synthetics for the same incidence geometry. Slopes of 15°–22° are required to explain our most anomalous observations.

To more realistically approximate the CMB conditions, synthetics are then generated with a ramp-like topography separating flat regions. The topography is analytically described by the relation

$$\Delta h(x) = a \times \tan^{-1}\left(\frac{x}{w}\right). \tag{3}$$

$\Delta h(x)$ expresses the elevation from average depth of any point of the seismic interface in the Cartesian (X, Y) plane. The shape of the structure is controlled by parameters a and w which represent the topographic relief (a) and, approximately, half the lateral extent of the structure (w). The slope is

$$d\Delta h/dx = \frac{a}{w\left(1+\frac{x^2}{w^2}\right)}, \tag{4}$$

which allows us to test the polarization rotation dependence on the lateral scale of the structure. In particular we investigated ramp topography models with a constant maximum slope ≈22°. The results are shown in Figs 11(c) and (d).

Ramps also induce *SKS* polarization rotation in ways similar to sloping interfaces if the ray piercing point is centred on the ramp. The polarization rotation increases with increasing separation between the backazimuth and the ramp's downdip direction (except for the along-strike direction). However, the magnitude of the rotation also depends on the lateral scale of the ramp. For 2 s period synthetics, and maximum interface slope of about 22°, significant rotations are caused by structures with lateral scales >200 km. Ramp widths of at least 350 km are necessary to remove any dependence on incidence geometry and generate the range of observed rotations seen in our *SKS* observations. The results approximate the ray-theoretic results for a dipping planar interface when the ramp width widens. At longer periods, lateral scale lengths >500–700 km are required to yield the range of polarization rotations we see in the *SKS* observations if the backazimuth is favourable.

The final two topography variants we explored were a ridge and a hill model. For both, the topographic uplift Δh was Gaussian, which, in the case of the ridge, was a function of one Cartesian coordinate x only, whereas for the hill, it was a function of $r = \sqrt{x^2 + y^2}$. For either,

$$\Delta h(x \text{ or } r) = 2a \exp\left(-(x \text{ or } r)^2/\sigma^2\right), \tag{5}$$

where σ is equal to $\frac{1}{4}$ the structure's total width. The resulting polarization rotations are summarized in Figs 12(a) and (b) for structures with topographic centre offset at $(\sigma, 0)$ and 2 s period synthetics. Only when lateral changes in elevation extend over 500 km do significant rotations arise. Furthermore, ridges generate polarization rotations more effectively than hills. However, rotations in the observed range are only achieved if the lateral scales exceed 1200 km and only from significant backazimuth deviations from the downdip direction.

These results also explain why *SKS* polarization is not affected by the Earth's ellipticity. In principle, poleward polarization rotations should arise due to increased CMB slope in those directions arising from polar flattening. Stacey (1992) provides formulae for the radial dependence on latitude ϕ in an elliptical earth, given flattening f (= 1/298.257) and equatorial radius a (= 6378.136 km),

$$r = a\left(1 + \frac{f(2-f)}{(1-f)^2}\sin^2\phi\right)^{-1/2}, \tag{6}$$

and

$$\frac{dr}{d\phi} = -a\left(1 + \frac{f(2-f)}{(1-f)^2}\sin^2\phi\right)^{-3/2}\left[\frac{f(2-f)}{(1-f)^2}\sin\phi\cos\phi\right]. \tag{7}$$

$\frac{dr}{d\phi}$ is largest near $\phi = \pi/4$, where it is $-a(1+\frac{f(2-f)}{2(1-f)^2})^{-3/2}(\frac{f(2-f)}{2(1-f)^2})$, or no more than 21.6 km rad^{-1} ≈ 0.12°. Thus, slopes as gentle as those induced by ellipticity would have a negligible influence on polarization rotations.

4.2.3 Interface properties

The synthetics thus far investigated use the properties of the CMB for the conversion interface, implying that CMB topography is the source of the anomalies in *SKS* and *SKKS* polarizations. An alternative mechanism to generate topography near the CMB is an ultra-low velocity zone (ULVZ) that varies in thickness. In order to make a quick assessment of the effect of ULVZ properties on the strength of polarization rotations, we will make use of the plane-wave reflection coefficients for the *P*-to-*S* conversion at the CMB and at a typical ULVZ structure and compare their relative strength. We seek

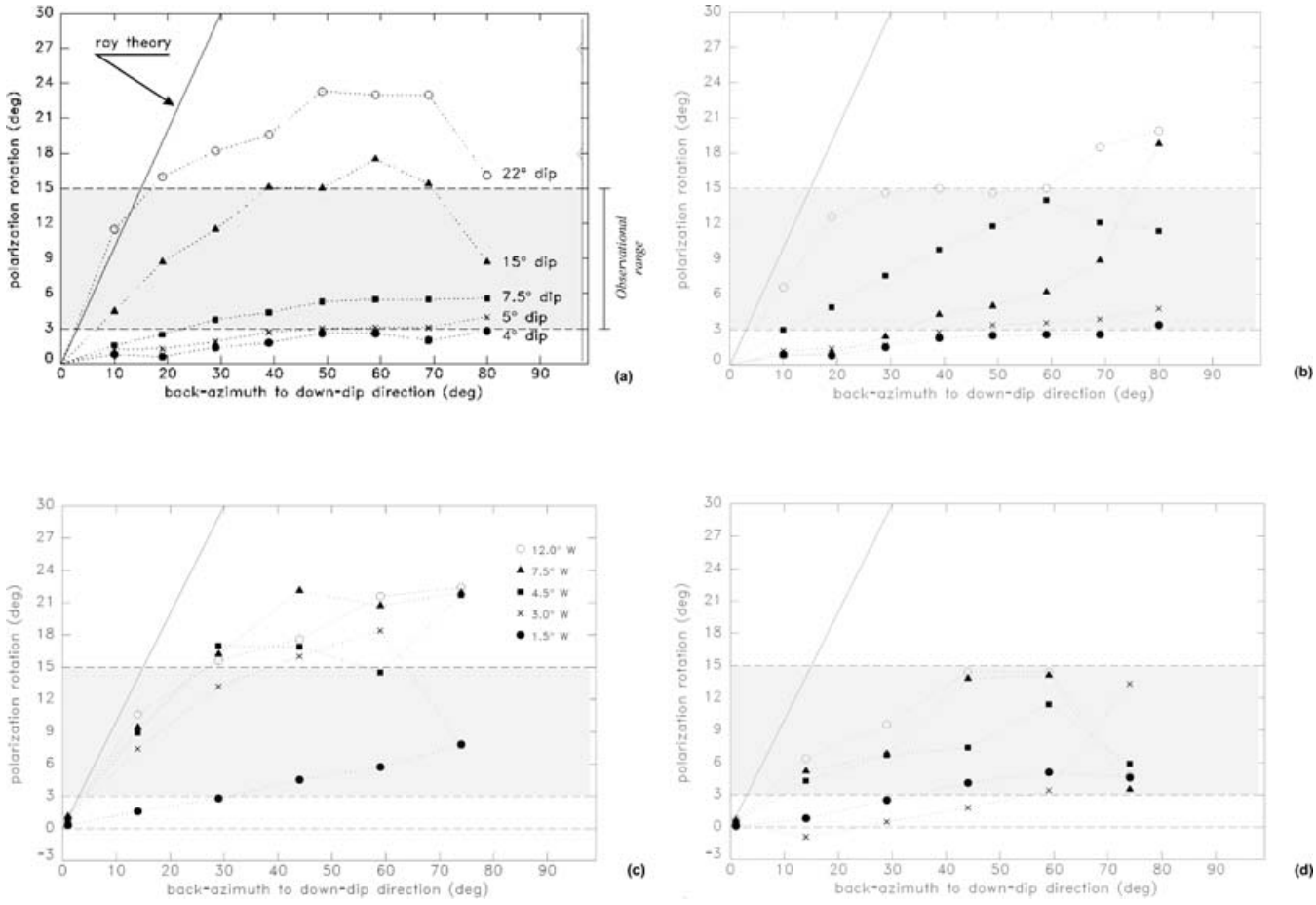

Figure 11. Results of polarization deviation analysis of synthetic seismograms converted from *P* to *S* at dipping flat discontinuities (a, b) and at finite-width ramp-like discontinuities (c, d). Increasing slopes are tested in the first case while maximum slope of the ramp discontinuity is constant in all such profiles but absolute dimensions vary (elevation range a and half-width w). Plots summarize 2-s (a, c) and 8-s (b, d) period synthetics calculated for a variety of $\hat{e_r} - \hat{d}$ values. Shaded area represents range of observed polarization rotations in our data set.

a simple scaling relation applicable to the CMB results to estimate the effect of ULVZ topography on *SKS* and *SKKS* polarizations.

The ULVZ properties we use are V_p and V_s reductions of 10 per cent and 30 per cent, respectively relative to the bottom of the mantle (Helmberger *et al.* 1998), with no change in density. For the appropriate slowness ranges for *SKS* and *SKKS*, we obtain ULVZ *P*-to-*S* transmitted amplitudes roughly 30 per cent of those calculated from CMB *P*-to-*S* transmission coefficients. It seems likely that polarization rotations would be small for ULVZ *P*-to-*S* conversions, because the converted waves would be relatively small contributions to the overall *SKS* or *SKKS* wavefield, so we do not explore them further.

4.2.4 Polarization rotation by velocity gradients

In anisotropic media, the *SH* and *SV* polarizations are coupled and do not propagate independently. One consequence of the coupling is a rotation of the *S* polarization vector around the ray propagation direction. The magnitude of the rotation is governed by the lateral gradient in wave speed and the difference between the group and phase velocity vectors, or, equivalently, the ray propagation direction and the energy propagation directions (Babuska & Cara 1991). This will rotate the initially *SV* polarized *SKS* or *SKKS* away from the source–receiver plane if it propagates through an anisotropic medium in which lateral gradients are present. Due to the known lateral heterogeneity in D″, the lateral gradients may rotate the *SKS* and *SKKS* polarizations to different degrees if their separation at the CMB exposes them to different areas of D″.

Hanyga (1988) describes the rotation ψ, which, in terms of our ray-centred coordinate frame (Fig. 10) is

$$\frac{d\psi}{dt} = -\frac{\hat{e_r}\cdot\mathbf{p}}{|\hat{e_r}\times\mathbf{p}|}\frac{\hat{e_r}\times\mathbf{p}}{|\hat{e_r}\times\mathbf{p}|}\cdot\nabla c, \tag{8}$$

where $\mathbf{p}$ is the slowness vector (wave front normal) and c is the wave speed. The relation shows that the rotation rate is zero if $\hat{e_r}$ is strictly perpendicular to $\mathbf{p}$, which is true in isotropic media. Furthermore, the $\hat{e_r}\times\mathbf{p}$ term yields a unit vector essentially parallel to the *SH* direction, indicating that rotation depends on the lateral velocity gradients, not the vertical ones.

To quantify the effect we need an estimate of the degree of non-perpendicularity of $\hat{e_r}$ and $\mathbf{p}$ in anisotropic media. Crampin (1982) provides the rule-of-thumb that the deviation angle between phase and group velocity ζ is $80\frac{\delta v}{v}$ (in degrees), where $\frac{\delta v}{v}$ is the fractional anisotropy. Thus, $\hat{e_r}\cdot\mathbf{p} \approx |\mathbf{p}|\sin(\zeta\pi/180)$ and $|\hat{e_r}\times\mathbf{p}| \approx |\mathbf{p}|$. Because ζ is small for a few percent anisotropy, $\frac{\hat{e_r}\times\mathbf{p}}{|\hat{e_r}\times\mathbf{p}|} \approx \hat{e_t}$. Thus a useful approximation is

$$\left|\frac{d\psi}{dt}\right| \approx \sin(\zeta\pi/180)\hat{e_t}\cdot\nabla c. \tag{9}$$

The travel time across a 200-km-thick D″ for *SKKS* at 103° is approximately 49 s. In order to get a rotation into the observed

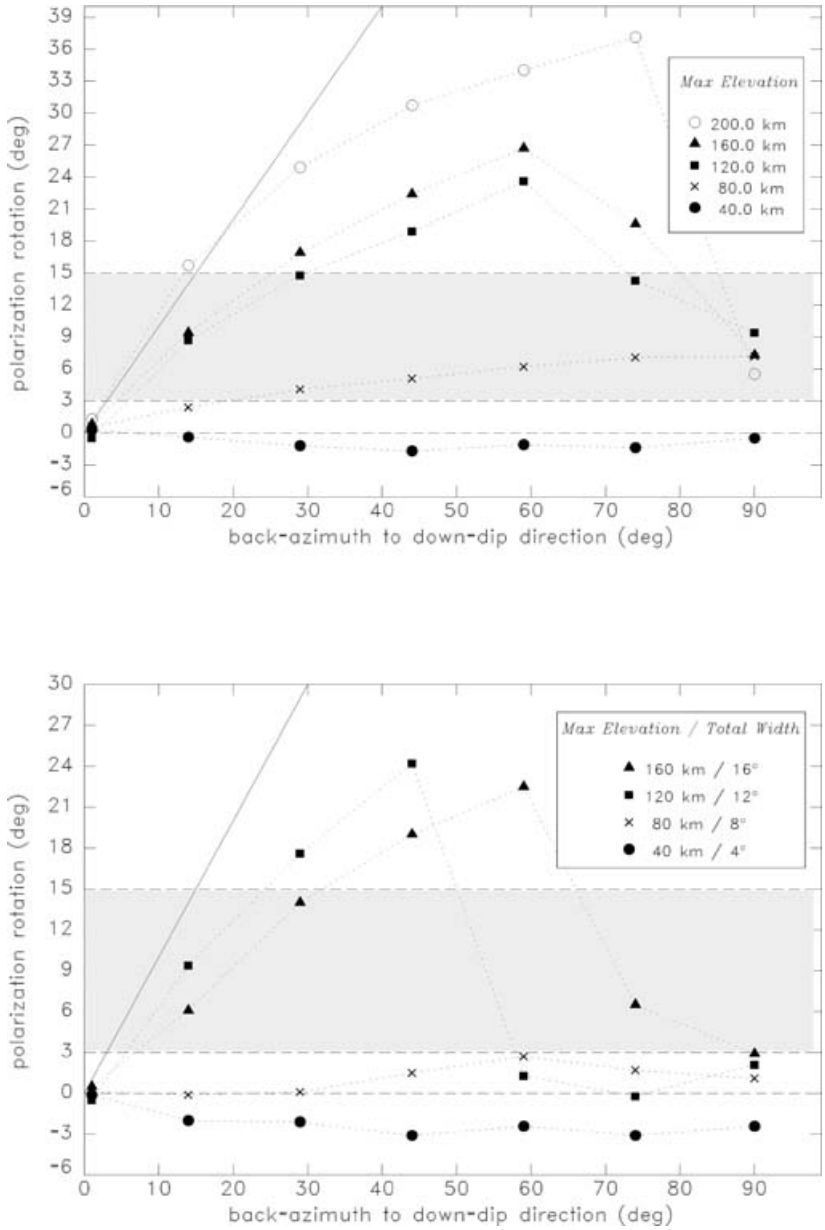

Figure 12. Results of polarization deviation analysis for more complicated topographies. Polarization rotations of synthetic *SKS* phases across ridge- (*top*) and dome-shaped (*bottom*) discontinuities of different widths. Topographic centre is at (W/2, 0) depending on half-width W of model itself. Slope at the geometric ray's incidence is constant for all models. All diagrams are for 2 s period synthetics.

range of $3^\circ \leq \psi \leq 15^\circ$ for 5 per cent anisotropy, we need a horizontal gradient $\nabla_h c$ of $0.015 \leq \nabla_h c \leq 0.770$ km s^{-1} km^{-1}. This is much larger than even the most extreme structural differences in D″ reported, those associated with ULVZs, which have 30 per cent ΔV_s over 200–500 km (Fig. 9), or $\nabla_h\, c < 0.011$ s^{-1}. Though lateral ULVZ gradients might be strong at the CMB, they do not extend through all of D″. Therefore, the known lateral gradients in D″ seem too weak to significantly rotate *SKKS* polarizations.

5 DISCUSSION

The anomalous splitting behaviour of *SKS* and *SKKS* phases we observed in our data set most likely arises from 2- or 3-D structure at the base of the mantle. Most areas of D″ sampled by our data are not anomalous, suggesting that they are either isotropic or contain a layer that exhibits hexagonally symmetric anisotropy with a vertical axis. Our preferred explanation of anomalous splitting is dipping discontinuities within D″ that affect the polarization of the $P \rightarrow S$ conversion. This mechanism is capable of generating the anomalous polarization rotations that we observe. If due to CMB topography, the slopes must be $>15^\circ$ and extend laterally more than 500 km, corresponding to angular order $\ell = 9$–18. Smaller-scale heterogeneity may also exist, but not be observable given the averaging scale of our method and the intrinsic limitations imposed by the width of *SKS* Fresnel zone at the CMB. (7.5°, i.e. roughly 450 km at the CMB, at epicentral distance of 120°). The anomalous areas imaged in our study appear to be anticorrelated with known ULVZs in D″. The anomalies we detect cluster geographically in areas of the CMB characterized by higher than average seismic velocities

(e.g. beneath North America and Central Asia), except eight phases only sampling a low-velocity area (northwestern Canada) which, at shorter wavelength, exhibits strong lateral variations of D″ structure (Garnero & Lay 1997).

One possible discontinuity in D″ is the post-perovskite transition in $MgSiO_3$ (Murakami *et al.* 2004; Shim *et al.* 2004). This appears to have a positive Clapeyron slope, leading to thicker D″ where temperatures are low and thinner where high. The observed anticorrelation between polarization anomalies and ULVZs at the CMB, where, presumably, temperatures are locally elevated, suggests that the anomalies arise in a cool, thick, post-perovskite rich D″. Polarization anomalies might arise due to large-scale topography on the phase boundary, or due to anisotropy changes (to a more general anisotropy than no or axis-vertical hexagonal) in the thicker D″ layer, with a stronger cumulative effect on *SKS* or *SKKS*. Neither of these two options is particularly attractive, however. There is only about a 1 per cent density change and a 4 per cent shear wave speed change in the material (Iitaka *et al.* 2004), much smaller than the contrast we need for topographically generated polarization changes. Our observations showed that any general non-VTI anisotropy in D″ must be smaller than 2 per cent. If a post-perovskite rich D″ were more strongly anisotropic (Tsuchiya *et al.* 2004), there must also be some mechanism to suppress it except in the few areas where we find anomalous splitting. It is not clear to us what this might be, though texturing developed during convective flow is a possibility (Iitaka *et al.* 2004; Garnero *et al.* 2004). Dislocation creep occurring in $MgSiO_3$ perovskite is referred to as a possibility to locally generate LPO-type anisotropy in the lower mantle by Perez & Niu (2004). Not enough is yet known about the slip systems in post-perovskite $MgSiO_3$ to assess this. Systematic investigations of the effects of different styles of lower mantle anisotropy through effective-medium and advanced waveform modelling have been recently conducted (Kendall & Silver 1998; Hall *et al.* 2004). Both SPO and LPO plausible structures are tested within constraints imposed by the physical properties of lowermost mantle mineral aggregates and current seismic observations. The degree of splitting produced by most models is small and comparable to the crust-induced one ($<$0.5 s). Only two models (melt-filled vertically aligned disk-shaped inclusions and horizontally aligned periclase) would produce significant splitting and discrepancies in *SKS* and *SKKS* behaviour. The former fabric could develop in hotter than average regions of D″. However, with the exception of our anomalous FRB record, we don't generally observe strong anomalies in correspondence of low-velocity areas. Due to our observation that anomalous differential splitting is restricted to non-ULVZ regions, periclase, horizontally aligned by lateral flows at downwelling points on the CMB, may be the anomalies' cause.

Alternatively, D″ structure might not be the cause of the anomalous polarizations that we observe, but topography on the CMB. The topography required, however, is greater than 50 km over lateral distances of 500 km, very much exceeding the values so far inferred, although at very long wavelengths ($>$1000 km), from tomographic inversions of *PcP*, *PKP* and *PKKP* residuals ($\pm$8 km CMB depth variation, Creager & Jordan (1986); $\pm$5 km, Morelli & Dziewonski (1987); $\pm$4 km, Doornbos & Hilton (1989); $\pm$1.5 km, Sze & van der Hilst (2003)). In the latter, recent and updated such study, inversion of separate subsets yields larger amplitude variations up to 5 km for all data except *PKPdf* data which yield instead 13 km. However, models inferred from *PcP* and *PKP/PKKP* sets alone are not consistent with each other, suggesting that residuals cannot be explained solely by CMB topography but shorter scale, lateral velocity variations in D″ as large as $\pm$5 per cent are also present. Such large topographies, and even more so our inferred values, are in contrast with evidence from total gravity field and geoid observations: Hager *et al.* (1985) at most allow for 3 km dynamically maintained CMB surface deformation at degree 2–3 spherical harmonics. The boundary is uplifted in hotter regions, with lower than average seismic velocities, and it is downwarped in cold, presumably denser and more viscous areas of D″, where most of the polarization rotations that we detect occur. Higher degree terms may however reveal larger dynamic topography.

At very short lateral scales instead (2–50 km), Menke (1986) rules out any major boundary corrugations that would substantially reduce the amplitude variation with distance of short-period *PcP*. This parameter is not sensitive however to CMB features at larger ($>$100 km) scales, which may still exist. Small-scale inhomogeneities would also cause scattering phenomena and precursors to *PKP* arrivals. Strong heterogeneity (10–15 per cent rms velocity variation) in a very thin basal layer and on lateral scales of 10 km is found in D″ north of Tonga from observations of anomalously large *PKP* precursors (Vidale & Hedlin 1998). This area underlies a large-scale region of slower than average seismic velocity, and the inferred velocity reductions are likely due to the presence of partial melt. They do not correspond to the pattern of anomalous rotations confined to fast D″ regions, however. The observed precursors could alternatively derive from coherent reflections off a dipping planar interface; this area is very poorly sampled by our data set and we did not find any record with anomalous *SKS*/*SKKS* polarization from this patch of D″ to provide new evidence. Scatterers of *PKP* are also invoked within a highly heterogeneous D″ area beneath Central America (Niu & Wen 2001). Velocity or density heterogeneities, CMB topography or a combination of both may be responsible for scattering. If scattering is due to CMB topography alone, elevations of up to 4 km are required, smaller than *SKS*/*SKKS* polarization rotations need and at smaller lateral scales. Alternatively, the lateral *P*-wave velocity variations as large as 6 per cent over 5–120 km that Niu & Wen (2001) infer are strong enough to rotate polarization provided that the gradient extends through the whole thickness of D″, and that a similar gradient strength exists in *S* as well as in *P*. These caveats make the mechanism unlikely, though not impossible.

Topographic features as large as we require would affect the travel times of both core-reflected *PcP* and core-refracted *PKP* waves, and, possibly, Earth rotation. PcP phases would show more negative residual times while *PKP* would suffer increased delays. We could not analyse *PcP* phases bouncing off the CMB locations where *SKS*/*SKKS* polarization rotations originate in order to fully confirm or reject the topography hypothesis though, and doubt whether this would add further constraints beyond those found by Doornbos & Hilton (1989) or Sze & van der Hilst (2003). CMB topography might explain precursors to PKKP due to back scattering into the core by a rough CMB, but the topography is limited to few kilometres at most (Doornbos 1980, 1988). These estimates are in any case much smaller than the topography needed to explain the *SKS*/*SKKS* polarization anomalies. In contrast, observations of the Earth's spin axis nutation limits $\ell = 2$ topography on the CMB to be smaller than $\sim$500 m (Gwinn *et al.* 1986; Wahr & de Vries 1989), but it could be larger at higher angular orders bracketing the scale we need to rotate *SKS* or *SKKS*. Thus, while short-period body wave travel time constraints favour small CMB topography, space geodetic constraints are insensitive to the scale of our observations.

Thus we are left with two unsatisfactory explanations for our observations: CMB topography or unusual anisotropy characteristics in particular areas. In the balance, unusual anisotropy seems more likely because it is more compatible with seismological constraints,

and on account of our ignorance of D″ phenomena and the high degree of lateral variability of physical properties and the possibility of complex dynamics in D″.

The exercise shows, however, that *SKS* and *SKKS* splitting anomalies arise due to polarization differences between *SKS* and *SKKS* before they enter the upper mantle, and that significant topography on a boundary with a significant velocity contrast can produce them. With more dense coverage of areas of the CMB either with regional arrays, or by using horizontally travelling rays in D″ to investigate azimuthal anisotropy in the anomalous areas of D″ (Garnero *et al.* 2004), there should be a clearer verdict rendered on the origins of anomalous splitting.

6 CONCLUSIONS

We documented different splitting behaviour in seismograms containing both *SKS* and *SKKS* at global sites. *SKS* and *SKKS* should be similarly split in a spherically symmetric earth with anisotropy confined to the upper mantle only. The origin of these discrepancies is attributed to heterogeneity in D″ where the ray paths for the two waves diverge significantly. The delay times between the fast and slow S-wave polarizations is, within measurement uncertainty, the same for *SKS* and *SKKS*, ruling out path-length effects in an anisotropic upper mantle or D″ as the origin of the splitting anomalies. The similarity of δt for split *SKS* and *SKKS* limit azimuthal anisotropy in D″ to be less than 2 per cent globally. The preferred explanation for the anomalous splitting is different polarizations for *SKS* and *SKKS*, which we measured and documented, ranging up to 20°. Through synthetics, we explored one model for how polarization rotations arise—topography on the core–mantle boundary—and determined the minimum topography required to explain the observed polarization rotations: 50 to a few hundreds km over length scales of 500–1000 km. The map of anomalous *SKS*/*SKKS* polarization rotations indicates that anomalies mostly occur in faster than average regions, away from ULVZs. A more likely, but as-yet untestable model for the anomalies we observe is locally unusual, but not widespread, anisotropy in D″.

ACKNOWLEDGMENTS

This work was funded by NERC studentship GT4/96/33 and an University of Bristol Research Fellowship to A. Restivo in pursuit of a PhD degree (1996–2002). We thank Mike Kendall for contributing data and comments on earlier phases of the project, Suzan van der Lee for the Kirchhoff code, and Justin Revenaugh for the ULVZ maps. Some data used in this study were obtained from IRIS DMC. Vernon Cormier and an anonymous reviewer provided useful remarks and suggestions to improve the manuscript. We thank the Dept. Centro di Ricerche Sismologiche of the Ist. Naz. di Oceanografia e di Geofisica Sperimentale, Trieste, Italy, for support to complete this paper.

REFERENCES

Babuska, V. & Cara, M., 1991. *Seismic anisotropy in the Earth*, Kluwer Academic, Dordrecht, Netherlands.

Barruol, G., Helffrich, G. & Vauchez, A., 1997. Shear wave splitting around the northern Atlantic: frozen Pangaean lithospheric anisotropy?, *Tectonophysics,* **279,** 35–148.

Bullen, K.E., 1949. Compressibility-pressure hypothesis and the Earth's interior, *Mon. Not. R. Astr. Soc.,* **5,** 355–368.

Cerveny, V., 2001. *Seismic Ray Theory*, Cambridge, Cambridge, UK.

Crampin, S., 1982. Comments on 'Possible forms of anisotropy of the uppermost mantle under oceans' by George E. Backus, *J. geophys. Res.,* **87,** 4646–4640.

Creager, K. & Jordan, T., 1986. Large-scale structure of the outermost core from P'df and P'ab travel times, in *EOS, Trans. Am. geophys. Un.*, Vol. 67, p. 311, AGU.

Doornbos, D.J., 1980. The effect of a rough core-mantle boundary on PKKP, *Phys. Earth Planet. Inter.,* **21,** 351–358.

Doornbos, D.J., 1988. Multiple scattering by topographic relief with application to the core-mantle boundary, *Geophys. J. Int.,* **92,** 465–478.

Doornbos, D.J. & Hilton, T., 1989. Models of the core-mantle boundary and the travel times of internally reflected core phases, *J. geophys. Res.,* **94,** 15 741–15 751.

Earle, P.S. & Shearer, P.M., 1997. Observations of PKKP precursors used to estimate small-scale topography on the core-mantle boundary, *Science,* **277,** 667–670.

Fouch, M.J. & Fisher, K.M., 1996. Mantle anisotropy beneath northwest Pacific subduction zones, *J. geophys. Res.,* **101,** 15987–16002.

Garnero, E.J. & Helmberger, D.V., 1995. A very slow basal layer underlying large-scale low velocity anomalies in the lower mantle beneath the Pacific: evidence from core phases, *Phys. Earth Planet. Inter.,* **91,** 161–176.

Garnero, E.J. & Lay, T., 1997. Lateral variations in the lowermost mantle shear wave anisotropy beneath the north Pacific and Alaska, *J. Geophys. Res.,* **102,** 8121–8135.

Garnero, E.J. & Lay, T., 2003. D″ shear velocity heterogeneity, anisotropy and discontinuity structure beneath the Caribbean and Central America, *Phys. Earth Planet. Inter.,* **140,** 219–242.

Garnero, E.J., Maupin, V., Lay, T. & Fouch, M.J., 2004. Variable azimuthal anisotropy in Earth's lowermost mantle, *Science,* **306,** 259–261.

Gutenberg, B. & Richter, C.F., 1939. On seismic waves, *Beitr. Geophys.,* **54,** 94–136.

Gwinn, C.R., Herring, T.A. & Shapiro, I.I., 1986. Geodesy by radio interferometry: Studies of forced nutations of the Earth 2. Interpretation, *J. geophys. Res.,* **92,** 4755–4765.

Haddon, R.A.W. & Buchen, P.W., 1981. Use of Kirchhoff's formula for body wave calculations in the Earth, *Geophys. J. R. astr. Soc.,* **67,** 587–598.

Hager, B.H., Clayton, R.W., Richards, M.A., Comer, R.P. & Dziewonski, A.M., 1985. Lower mantle heterogenity, dynamic topography and the geoid, *Nature,* **313,** 541–545.

Hall, S.A., Kendall, J.M. & van der Baan, M., 2004. Some comments on the effects of lower-mantle anisotropy on SKS and SKKS phases, *Phys. Earth planet. Inter.,* **146,** 469–481.

Hanyga, A., 1988. Numerical tracing of rays and wavefronts, in *Seismological Algorithms*, pp. 169–233, ed. Doornbos, D., Academic Press, London, UK.

Hedlin, M.A.H., Shearer, P.M. & Earle, P.S., 1997. Seismic evidence for small-scale heterogeneity throughout the Earth's mantle, *Nature,* **387,** 145–150.

Helmberger, D.V., Wen, L. & Ding, X., 1998. Seismic evidence that the source of the Iceland hotspot lies at the core-mantle boundary, *Nature,* **396,** 251–255.

Holme, R., 1998. Electromagnetic core-mantle coupling II: probing deep mantle conductance, in *The core-mantle boundary region*, Vol. 28, pp. 139–151, eds Gurnis, M., Wysession, M.E., Knittle, E. & Buffett, B.A., Geodynamics series, AGU, Washington, D.C.

Iitaka, T., Hirose, K., Kawamura, K. & Murakami, M., 2004. The elasticity of the $MgSiO_3$ post-perovskite phase in the Earth's lowermost mantle, *Nature,* **430,** 442–445.

Kendall, J.M. & Nangini, C., 1996. Lateral variations in D″ below the Caribbean, *Geophys. Res. Lett.,* **23,** 399–402.

Kendall, J.M. & Silver, P.G., 1996. Constraints from seismic anisotropy on the nature of the lowermost mantle, *Nature,* **381,** 409–412.

Kendall, J.-M. & Silver, P.G., 1998. Investigating causes of D″ anisotropy, in *The core-mantle boundary region*, Vol. 28, pp. 97–118, eds Gurnis, M., Wysession, M.E., Knittle, E. & Buffett, B.A., Geodynamics series, AGU, Washington, D.C.

Kennett, B.L.N. & Engdahl, E.R., 1991. Traveltimes for global earthquake location and phase identification - IASP91 model, *Geophys. J. Int.,* **105,** 429–465.

Knittle, E., 1998. The solid/liquid partitioning of major and radiogenic elements at lower mantle pressures: implications for the core-mantle boundary region, in *The core-mantle boundary region*, Vol. 28, pp. 119–130, eds Gurnis, M., Wysession, M.E., Knittle, E. & Buffett, B.A., Geodynamics series, AGU, Washington, D.C.

Kuo, B.Y., Garnero, E.J. & Lay, T., 2000. Tomographic inversion of S-SKS times for shear velocity heterogeneity in D″: degree 12 and hybrid models, *J. geophys. Res.,* **105,** 28 139–28 157.

Lay, T. & Helmberger, D.V., 1983. A lower mantle S-wave triplication and the shear velocity structure of D″, *Geophys. J. R. astr. Soc.,* **75,** 799–838.

Lay, T., Garnero, E.J., Young, C.J. & Gaherty, J.B., 1997. Scale lengths of shear velocity heterogeneity at the base of the mantle from S wave differential travel times, *J. geophys. Res.,* **102,** 9887–9909.

Loper, D.E. & Lay, T., 1995. The core-mantle boundary region, *J. geophys. Res.,* **100,** 6397–6420.

Meade, C., Silver, P.G. & Kaneshima, S., 1995. Laboratory and seismological observations of lower mantle isotropy, *Geophys. Res. Lett.,* **22,** 1293–1296.

Menke, W., 1986. Few 2-50 km corrugations on the core-mantle boundary, *Geophys. Res. Lett.,* **13,** 1501–1504.

Morelli, A. & Dziewonski, A.M., 1987. Topography of the core-mantle boundary and lateral homogeneity of the liquid core, *Nature,* **325,** 678–683.

Mori, J. & Helmberger, D.V., 1995. Localized boundary-layer below the mid-Pacific velocity anomaly identified from a PcP precursor, *J. geophys. Res.,* **100,** 20 359–20 365.

Murakami, M., Hirose, K., Kawamura, K., Sata, N. & Ohishi, Y., 2004. Post-perovskite phase transition in $MgSiO_3$, *Science,* **304,** 855–858.

Ni, S.D. & Helmberger, D.V., 2001. Horizontal transition from fast to slow structures at the core-mantle boundary: South Atlantic, *Earth planet. Sci. Lett.,* **187,** 301–310.

Niu, F. & Wen, L., 2001. Strong seismic scatterers near the core-mantle boundary west of Mexico, *Geophys. Res. Lett.,* **28,** 3557–3560.

Olivieri, M., Pino, N.A. & Morelli, A., 1997. Evidence for an S-velocity discontinuity in the lowermost mantle beneath the South Eastern Pacific Basin, *Geophys. Res. Lett.,* **24,** 2617–2620.

Owens, T.J., 1987. Crustal structure of the Adirondack mountains determined from broadband teleseismic waveform modeling, *J. geophys. Res.,* **92,** 6391–6401.

Perez, A.M. & Niu, F., 2004. Seismic anisotropy in the lower mantle: a comparison of waveform splitting of SKS and SKKS, in *EOS, Trans. Am. geophys. Un.*, **85**(47) in Fall Meet. Suppl., pp. Abstract T11E–1329, AGU.

Poirier, J.-P., Malavergne, V. & Mouel, J.L.L., 1998. Is there a thin electrically conducting layer at the base of the mantle?, in *The Core-Mantle Boundary Region*, Vol. 28, pp. 131–137, eds Gurnis, M., Wysession, M.E., Knittle, E. & Buffett, B.A., Geodynamics series, AGU, Washington, DC, USA.

Restivo, A. & Helffrich, G., 1999. Teleseismic shear wave splitting measurements in noisy environments, *Geophys. J. Int.,* **137,** 821–830.

Shim, S.-H., Duffy, T.S., Jeanloz, R. & Shen, G., 2004. Stability and crystal structure of $MgSiO_3$ perovskite to the core-mantle boundary, *Geophys. Res. Lett.,* **31,** art. no. L10603.

Sidorin, I. & Gurnis, M., 1998. Geodynamically consistent seismic velocity predictions at the base of the mantle, in *The core-mantle boundary region*, Vol. 28, pp. 209–230, eds Gurnis, M., Wysession, M.E., Knittle, E. & Buffett, B.A., Geodynamics series, AGU, Washington, D.C.

Silver, P.G., 1996. Seismic anisotropy beneath the continents: probing the depth of geology, *Ann. Rev. Earth Planet. Sci.,* **24,** 385–432.

Silver, P.G. & Chan, W.W., 1991. Shear wave splitting and sub-continental mantle deformation, *J. geophys. Res.,* **96,** 16 429–16 454.

Stacey, F.D., 1992. *Physics of the Earth*, Brookfield Press, Brisbane.

Sze, E.K.M. & van der Hilst, R.D., 2003. Core mantle boundary topography from short period PcP, PKP and PKKP data, *Phys. Earth planet. Inter.,* **135,** 27–46.

Tackley, P.J., 1998. Three-dimensional simulations of mantle convection with a thermo-chemical basal boundary layer: D″?, in *The core-mantle boundary region*, Vol. 28, pp. 231–253, eds Gurnis, M., Wysession, M.E., Knittle, E. & Buffett, B.A., Geodynamics series, AGU, Washington, D.C.

Thomas, C., Weber, M., Wicks, C.W. & Scherbaum, F., 1999. Small scatterers in the lower mantle observed at German broadband arrays, *J. geophys. Res.,* **104,** 15 073–15 088.

Thomas, C., Kendall, J.-M. & Weber, M., 2002. The lowermost mantle beneath northern Asia - I. Multi-azimuth studies of a D″ heterogeneity, *Geophys. J. Int.,* **151,** 279–295.

Tkalcic, H., Romanowicz, B. & Houy, N., 2002. Constraints on D″ structure using PKP(AB-DF), PKP(BC-DF) and PcP-P traveltime data from broadband records, *Geophys. J. Int.,* **149,** 599–616.

Tsuchiya, T., Tsuchiya, J., Umemoto, K. & Wentzcovitch, R.M., 2004. Elasticity of post-perovskite $MgSiO_3$, *Geophys. Res. Lett.,* **31,** art. no. L14603.

van der Lee, S., Paulssen, H. & Nolet, G., 1994. Variability of P660s phases as a consequence of topography of the 660 km discontinuity, *Phys. Earth planet. Inter.,* **86,** 147–164.

Vidale, J.E. & Hedlin, M.A.H., 1998. Evidence for partial melt at the core-mantle boundary North of Tonga from the strong scattering of seismic waves, *Nature,* **391,** 682–685.

Wahr, J. & de Vries, D., 1989. The possibility of lateral structure inside the core and its implications for nutation and Earth tide observations, *Geophys. J. Int.,* **99,** 511–519.

Williams, Q., Revenaugh, J. & Garnero, E., 1998. A correlation between ultra-low basal velocities in the mantle and hot spots, *Science,* **281,** 546–549.

Wookey, J., Kendall, J.-M. & Barruol, G., 2002. Mid-mantle deformation inferred from seismic anisotropy, *Nature,* **415,** 777–780.